

Contents lists available at ScienceDirect

International Journal of Engineering Science

journal homepage: www.elsevier.com/locate/ijengsci



Hyperelastic constitutive modeling of hydrogels based on primary deformation modes and validation under 3D stress states



Kshitiz Upadhyay, Ghatu Subhash*, Douglas Spearot

Department of Mechanical and Aerospace Engineering, University of Florida, Gainesville, FL 32611, USA

ARTICLE INFO

Article history: Received 9 December 2019 Revised 27 April 2020 Accepted 29 April 2020 Available online xxx

Keywords:
3D constitutive model
Rubber elasticity
Mechanical testing
Digital image correlation (DIC)
Finite element analysis
Agarose hydrogel

ABSTRACT

In isotropic linear elasticity, a constitutive model calibrated using a single deformation mode (e.g., compression or tension or shear) is sufficient to describe a complex threedimensional (3D) stress state. Such an approach, however, is likely inadequate for modeling hydrogels, which exhibit a nonlinear stress-strain response that varies significantly between deformation modes and is also sensitive to microstructure via gel concentration. In this study, a combined experimental and constitutive modeling framework is proposed for the development and validation of concentration-dependent 3D hyperelastic models for hydrogels. Agarose hydrogel in a concentration range of 0.4-4% w/v is chosen as the model material. Uniaxial compression, uniaxial tension, and simple shear (three primary deformation modes) experiments are conducted. The small strain elastic modulus-gel concentration relationships obtained from experiments are compared with those predicted by the molecular theory of rigid polymer networks (Jones-Marques theory) to identify the concentration range in which entropic elastic (hyperelastic) response dominates. In this range (1.5-4% w/v), four hyperelastic constitutive models are fit to the combined compressiontension-shear stress-strain data: Mooney-Rivlin, three-parameter generalized Rivlin, Gent, and Gent-Gent models. It is demonstrated that the generalized Rivlin model offers the best overall accuracy, and the variation of its model parameters with gel concentration is consistent with the Jones-Marques theory. The resulting concentration-dependent Extended Generalized Rivlin model is employed in finite element simulations of the nonhomogeneous 3D stress state of wedge indentation. Simulated load versus depth and strain field predictions show very good agreement with experimental wedge indentation results. Finally, it is shown that a hyperelastic model calibrated using only a single deformation mode yields poor results for other primary and 3D deformations, and thus multiple primary deformation modes (preferably all three) should be considered.

© 2020 Elsevier Ltd. All rights reserved.

1. Introduction

Hydrogels are polymeric materials that swell in an aqueous medium and form stable three-dimensional networks. Owing to their characteristic hydrophilicity and porous microstructure similar to that of many biological tissues, hydrogels are

E-mail address: subhash@ufl.edu (G. Subhash).

^{*} Corresponding author.

known to possess biocompatibility and biomimetic properties. From a mechanics perspective, they are soft materials that can undergo large nonlinear deformations without failure. Because of such unique properties, hydrogels have been successfully employed in a number of applications, such as soft contact lenses (Hyon et al., 1994), drug-delivery systems (Lin & Anseth, 2009), tissue phantoms (Maxwell et al., 2010), tissue engineering implants/scaffolds (El-Sherbiny & Yacoub, 2013; Ma, 2004; Peattie et al., 2004), and sensors and actuators (Trinh, Sorber & Gerlach, 2009). A comprehensive understanding of the mechanical behavior of hydrogels is vital for the effective design of these systems.

Numerous small strain and large deformation studies on hydrogels exist in the literature. The former utilize shear rheometry, dynamic mechanical analysis (DMA), ultrasonic measurements, etc., to obtain the elastic modulus (uniaxial, bending or shear; storage, loss, complex, etc.) (Clark & Ross-Murphy, 1987). Many large deformation studies use a traditional universal testing frame and/or a split Hopkinson pressure bar to report elastic moduli, failure stresses, and failure strains in a variety of loading conditions and strain rate regimes (Chen, 2016; Clark & Ross-Murphy, 1987). These traditional "linear elastic" material properties have offered important power law (scaling) relationships with various microstructural and loading parameters (e.g., see (Buckley, Thorpe, O'Brien, Robinson & Kelly, 2009; Q. Chen, Suki & An, 2004; Forte, Galvan, Manieri, Rodriguez y Baena & Dini, 2016; Guenet, 2000; Hinkley, Morgret & Gehrke, 2004; Kim, Kim, Gunasekaran, Park & Yoon, 2013; Moura, Figueiredo & Gil, 2007; Normand, Lootens, Amici, Plucknett & Aymard, 2000; Rinaudo, 1993; Subhash, Liu, Moore, Ifju & Haile, 2011; Watase & Nishinari, 1983)). However, little insight is obtained in terms of modeling the entire stress-strain behavior because unlike linear elastic materials, hydrogels' stress-strain data is nonlinear and cannot be completely characterized based on only its initial and final (yield or failure) points.

To describe the nonlinear deformation behavior of hydrogels, hyperelasticity offers an attractive constitutive modeling framework (Wex, Arndt, Stoll, Bruns & Kupriyanova, 2015). These models assume a time-independent and fully reversible deformation with no energy dissipation (entropic elasticity), which are reasonable assumptions especially under low loading rates and in certain ranges of temperature and gel concentration (Oyen, 2014; Upadhyay, Subhash & Spearot, 2020). Consequently, many recent studies have used hyperelastic models to fit the stress-strain data of hydrogels under uniaxial compression (Castilho et al., 2018; Faturechi, Karimi, Hashemi, Yousefi & Navidbakhsh, 2015; Leclerc et al., 2012; Naarayan & Subhash, 2017; Pavan, Madsen, Frank, Adilton O Carneiro & Hall, 2010; Sasson, Patchornik, Eliasy, Robinson & Haj-Ali, 2012), uniaxial tension (Agnelli, Baldi, Bignotti, Salvadori & Peroni, 2018; Mathews, Birney, Cahill & McGuinness, 2008; Trinh et al., 2009), torsion (Tang, Tung, Lelievre & Zeng, 1997), and indentation (Moerman, Holt, Evans & Simms, 2009). A common feature in most of these studies is the consideration of a single homogeneous deformation mode (e.g., only compression, only tension, etc.) in the determination of hyperelastic model parameters. This is likely because conducting experiments under many different deformation modes on these soft, slippery and fragile materials is difficult and sometimes infeasible owing to the complexities related to specimen mounting, edge effects, stress/strain-field measurement, homogeneity validation, etc. (Luo et al., 2019; Upadhyay, Bhattacharyya, Subhash & Spearot, 2019).

Consideration of a single deformation mode in calibrating hyperelastic models for hydrogels, although a common practice, can severely limit the model's applicability in real-world mechanics problems. For example, Normand et al. (Normand et al., 2000) showed that agarose hydrogels exhibit significantly different mechanical behaviors under compression and tension, with the former deformation mode resulting in higher elastic modulus, failure stress and failure strain. Additionally, compression response showed greater nonlinearity when compared to tensile response. This type of asymmetric mechanical behavior among different deformation modes was also noticed by Pasumarthy and Tippur (Pasumarthy & Tippur, 2016) in ballistic gelatin and by Tang et al. (Tang et al., 1997) in gellan gels. These studies suggest that a hyperelastic model based on a particular deformation mode (say compression) may not accurately capture a different deformation mode (say tension) or a general triaxial stress state that consists of a complex combination of compression, tension and shear components. In addition to the asymmetric mechanical behavior, the nonlinearity of stress-strain data can also lead to multiple optimal model parameters from different deformation modes, thus resulting in poor model performance in deformation modes other than the one used for calibration (Ogden, Saccomandi & Sgura, 2004). In a more recent study, Upadhyay et al.(Upadhyay et al., 2019b) showed that the bounds of allowable hyperelastic model parameters depend on the deformation mode under consideration, and experiments covering all three primary deformation modes (compression, tension and shear) should be conducted to ensure thermodynamic stability of the model under a general triaxial deformation state. Clearly, the formulation of hyperelastic models for hydrogels that consider multiple primary deformation modes and are transferrable into complex loading conditions is much needed. This should also be accompanied with a careful consideration of the microstructural parameters (e.g., crosslinking density and network mesh size) on which the mechanical response of hydrogels is intimately dependent.

With this motivation, the present study aims to develop an experimental characterization and constitutive modeling framework for the study of the mechanical response of hydrogels under multiple deformation modes and as a function of their molecular structure (via gel concentration). To this end, agarose gel is chosen as a model material, which is a thermoreversible physically cross-linked hydrogel used as a tissue culture medium (Chen et al., 2004b) and brain tissue surrogate owing to its comparable density and mechanical properties (Deepthi et al., 2010; Pervin & Chen, 2011; Pomfret, Miranpuri & Sillay, 2013). The uniaxial compression experiment is the most commonly performed experiment on hydrogels, and in this work is conducted on a number of different polymer concentration samples (0.4, 0.75, 1, 1.5, 2.5 and 4% w/v) to establish the range of concentrations where an entropic (hyperelastic) elastic response dominates. Once such a concentration range is identified, uniaxial tension and simple shear experiments are conducted in this range using custom-manufactured test fixtures. Digital image correlation (DIC) is used for full-field strain measurement during the experiments. The stress-strain data

from all three primary deformation modes is used to calibrate four hyperelastic models: the polynomial Mooney-Rivlin and three-parameter generalized Rivlin models (Mooney, 1940; Rivlin, 1948), and the exponential/logarithmic Gent (Gent, 1996) and Gent-Gent (Pucci & Saccomandi, 2002) models. The various hyperelastic models are compared on the basis of their fitting accuracy as well as the evolution of their model constants with gel concentration. A gel concentration dependent as well as network mesh size dependent (via appropriate scaling relations) extended hyperelastic model is formulated. The applicability of this model under complex deformations is validated via a non-homogeneous triaxial deformation state of wedge indentation. Finite element (FE) simulation outputs are compared with experimental test results. Finally, model insufficiencies arising from the consideration of fewer experimental deformation modes are investigated.

2. Materials and experimental methods

Four mechanical experiments: uniaxial compression, uniaxial tension, simple shear, and wedge indentation, are conducted on agarose hydrogels. Uniaxial compression is conducted on samples with six different polymer concentrations: 0.4, 0.75, 1.0, 1.5, 2.5 and 4% w/v. Upon confirming entropic elasticity in high concentration gels, uniaxial tension and simple shear experiments are conducted only on 1.5, 2.5 and 4% w/v samples. Various hyperelastic models are then fit to the combined tension, compression and shear data. To validate the suitability of the chosen constitutive model, wedge indentation experiments are conducted on a gel block of 3% w/v concentration (different from those used to calibrate the hyperelastic models). The strain fields during the experiment are mapped using DIC and then compared to the finite element model results.

2.1. Agarose gel structure and sample preparation

The agarose molecule is a linear polysaccharide consisting of β -1,3 linked D-galactose and α -1,4 linked 3,6-anhydro- α L-galactose residues (Normand et al., 2000). When cooled from a homogeneous aqueous solution at 80–90 °C to a temperature below its gelation temperature (~35 °C), it forms a three-dimensional network of physically cross-linked agarose fibers. Thermodynamically, this gelation involves transformation from a random coil configuration in sol state to a double helix in the initial stages. Between 10 and 10⁴ helices bundle to form fibrils, which aggregate to form the polymer network in the final gel state (Ratajska-Gadomska & Gadomski, 2004). Different aspects of the network structure (crosslinking density, mesh size, etc.) are determined by the initial gelling parameters such as gel concentration, average molecular weight of the polymer, and solvent ionic strength (Anseth, Bowman & Brannon-Peppas, 1996; Oyen, 2014). In the present study, all but the gel concentration parameter are kept fixed (deionized (DI) water solvent is used; expected value of weight average molecular weight based on the agarose gel concentration–molecular weight–elastic modulus measurements in Normand et al. (2000) is 162,000 g/mol). Thus, the microstructure changes only via gel concentration.

Agarose powder (< 0.15% sulfate) is purchased from Fisher Scientific (Pittsburgh, PA; cat. no. BP1356); DI water is purchased from PTI Process Chemicals (Ringwood, IL). To start, agarose powder is mixed with DI water (solvent) at different polymer concentrations (% w/v). The mixture is heated in a microwave oven with intermediate stirring every 30 s until a transparent homogeneous solution is obtained. Heating time varies from 5–10 min depending on the polymer concentration and solution volume. At this point, the weight of solution is measured, and additional water is added to compensate for any water loss due to evaporation. After further heating for 0.5–1 min, the clear solution is transferred to a pressure cooker, where it is kept under atmospheric pressure for 5–15 min to eliminate any bubbles. The resulting bubble-free solution is used to fabricate test specimens for the mechanical experiments. For cylindrical compression, dog-bone shaped tension, and cuboidal indentation test specimens, the gelation mixture (sol) is directly poured into custom-designed rubber/acrylic molds. For rectangular shear test specimens, a large sheet is first molded, from which specimens are cut using a custom-made "cookie" cutter. Test specimens are stored in DI water until testing; all tests are conducted within 30 min of gel formation to minimize evaporative water loss.

2.2. Mechanical testing

All tests (compression, tension, shear, and wedge indentation) are conducted at room temperature under displacement control on a dual column electro-mechanical universal testing machine (Frame 311, TestResources, Inc., Shakopee, MN) equipped with a 1.1 kN load cell (\pm 0.5% accuracy) using appropriate test fixtures. A constant strain rate of $10^{-3}~s^{-1}$ is employed. Three tests are conducted for each polymer concentration. Specific details pertaining to individual experiments are given in the following subsections.

2.2.1. Uniaxial compression

Fig. 1(a) shows the uniaxial compression test setup, which consists of a fixed and a movable flat steel platen. A cylindrical (25.4 mm dia. x 25.4 mm length) gel sample is sandwiched between the two platens; the top platen is lowered at 1.524 mm/min to impose an engineering strain rate of 10^{-3} s⁻¹. Load cell force and crosshead displacement outputs are used to calculate engineering stress and strain, respectively. As the present study is focused only on the bulk deformation response, the portion of the stress-strain plot beyond specimen failure is disregarded.

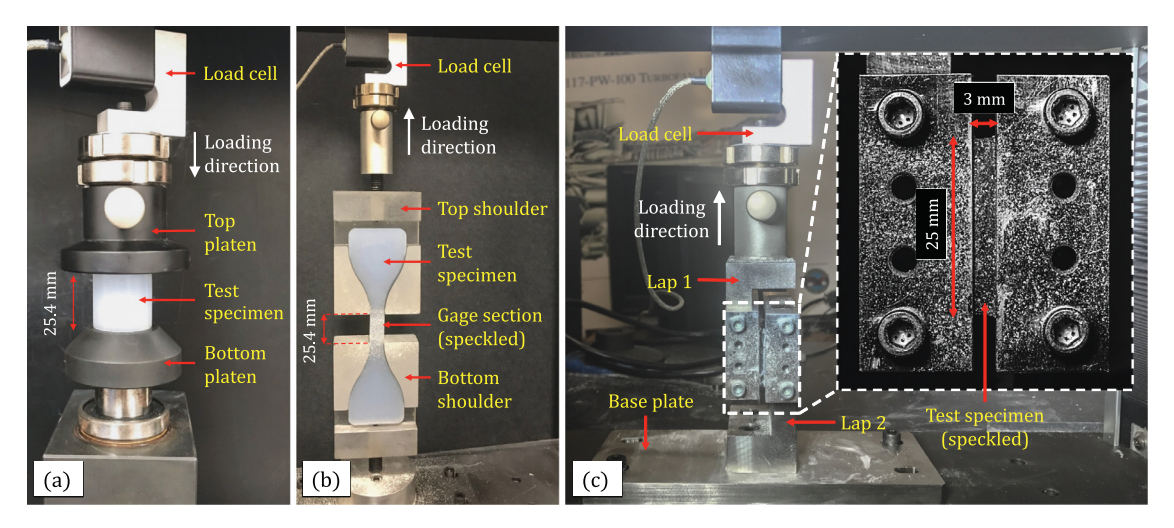


Fig. 1. Experimental setup for (a) uniaxial compression, (b) uniaxial tension, and (c) simple shear experiments on agarose gel. Inset in (c) shows a close-up monochromatic view of the lap plates and specimen (speckled using fine chalk powder).

2.2.2. Uniaxial tension

A tensile test fixture previously developed by Subhash et al. (Subhash et al., 2011) is used in this study, which is composed of two poly(methyl methacrylate) (PMMA) specimen holders between which a dog-bone shaped gel specimen is shoulder supported (Fig. 1(b)). The gage section dimensions are 25.4 mm x 12.7 mm x 12.7 mm. To impart a quasi-static strain rate of 10^{-3} s⁻¹, the top shoulder is pulled (via crosshead) at 1.524 mm/min. Similar to the compression test, the load cell force output is used to calculate the engineering tensile stress. Strain measurement, however, requires additional considerations, which are discussed in the following paragraph.

Strain measurement during mechanical testing of hydrogels (barring compression testing) is non-trivial owing to their soft, slippery and fragile nature. For example, the use of crosshead displacement to measure strain in these materials is not suitable due to the inevitable slippage near mounting/gripping areas. In these cases, the measurement of overall elongation or "average" strain may give erroneous results (Kwon, Rogalsky, Kovalchick & Ravichandran, 2010). In addition, traditional contact-based extensometers cannot be mounted on these materials because even a small amount of compressive mounting force (of say, clip extensometer) tends to excessively deform the soft gel sample at that location and may even initiate a crack (Subhash et al., 2011). Other contact-based strain measuring equipment (e.g., strain gages) also cannot be used because of the wet surfaces of these materials. To overcome these difficulties, digital image correlation (DIC) is used in the present study for tension, shear and indentation experiments, which is a non-contact optical strain measurement technique that maps full-field deformation by tracking movement of a randomly distributed speckle pattern on the sample gage surface.

Particularly for the uniaxial tension experiment, 3D DIC is used, which allows for measurement of both in-plane and out-of-plane displacements by stereo correlation of images captured from two cameras; 30 images of a standard calibration grid are used for calibration. Since hydrogels have a wet surface, hygroscopic fine chalk powder (100–300 μ m) is used to create the speckle pattern. Chalk particles do not separate or flow, and adhere well to the sample surface even during large deformations (Kwon et al., 2010). The speckled sample gage area is imaged (1 image every 3 s) using two 5.0 MP CCD cameras (GRAS-50S5M-C (Sony ICX 625 CCD), FLIR Sytems, Inc., Richmond, Canada). Both cameras are located horizontally such that their lines of sight cross at ~45° angle (~22.5° on either side of the sample surface normal). The camera resolution is 2448×2048 pixels and the spatial resolution is ~17 pixels/mm, such that approximately 434×217 pixels exist in the specimen gage area (25.4 mm x 12.7 mm). Images are analyzed using the commercial VIC-3D 6 software (Correlated Solutions, Inc., Irmo, SC), which provides the average axial engineering strain in the specimen gage section that is used to create the stress-strain plots. Note, subset size is selected for individual imaging data based on the speckle density and size (subset size > (3 x speckle size)), and also the sigma value (one standard deviation confidence interval) of the subset tracking function.

2.2.3. Simple shear

Single lap-shear experiments are conducted on a custom-built test fixture shown in Fig. 1(c), which consists of two L-shaped lap plates: a Lap-2 plate fixed to the machine base, and a Lap-1 plate that translates vertically to impart shear strain in the gel specimen. A rectangular prism shaped agarose gel specimen is bonded between the two lap plates using a thin layer of cyanoacrylate adhesive (Adhesive Systems Inc., Frankfort, IL; cat. no. M 60). Specimen dimensions are chosen as 25 mm x 3 mm x 10 mm, which follow the suggested inequalities for maximizing strain homogeneity and preventing shear buckling ((Upadhyay et al., 2019a)). Cyanoacrylate-based adhesives polymerize rapidly in the presence of water in hydrogels, confining the curing reaction to a thin ~100 μ m layer (Subhash, Kwon, Mei & Moore, 2012; Wang & Kornfield, 2012). The effect of adhesive diffusion on material response is thus neglected. Lap-1 (or crosshead) is translated vertically at a constant

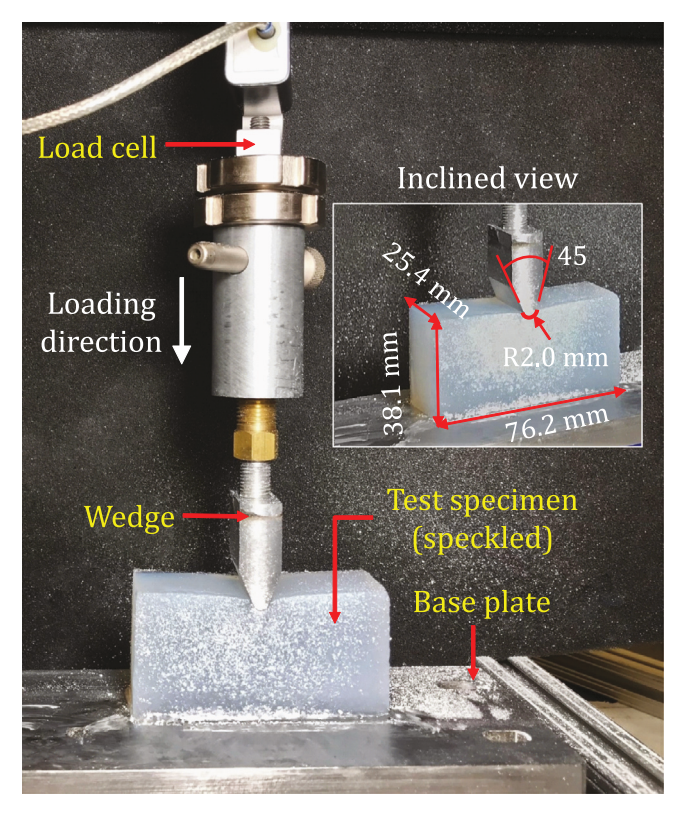


Fig. 2. Experimental setup for wedge indentation test. Inset shows an inclined close-up view with marked specimen and indenter dimensions.

velocity of 0.169 mm/min to ensure a 10^{-3} s⁻¹ loading strain rate. As no out-of-plane deformation of specimen gage section is allowed in simple shear deformation, 2D DIC is used for average shear strain measurement. A single 5.0 MP CCD camera is used to capture the deformation event at a rate of 1 image every 3 s. The spatial resolution is ~35 pixels/mm and thus approximately 105 pixels are along the gage section width (3 mm). Captured images are analyzed in the commercial Vic-2D 6 software (Correlated Solutions, Inc., Irmo, SC).

2.2.4. Wedge indentation

A custom-designed steel wedge is used to conduct indentation experiments on cuboidal agarose gel samples (76.2 mm x 38.1 mm x 25.4 mm) as shown in Fig. 2. The crosshead velocity is set to 2.286 mm/min to ensure a nominal loading strain rate of 10^{-3} s⁻¹. The total indentation depth is 2 mm. The load cell force and crosshead displacement outputs are used to create the indentation load-depth plots. 3D DIC via Vic-3D 6 software is used to measure the full-field strain across the sample surface with a measurement setup (camera specifications and orientation, calibration, speckle pattern, etc.) identical to the one used in tensile testing, except that the imaging frequency is increased to 1 Hz in response to the increased crosshead velocity. The spatial resolution is ~25 pixels/mm in the area of interest close to the indenter tip.

3. Constitutive modeling and finite element simulations

3.1. Hyperelastic modeling and fitting procedure

Initially developed to study the entropic elastic behavior of rubbers (refer to a detailed review by Anseth et al. (Anseth et al., 1996)), hyperelasticity has been successfully applied to describe the mechanical behavior of hydrogels (Sasson et al., 2012; Tang et al., 1997), biological tissues (Budday et al., 2017; Veronda & Westmann, 1970), additively manufactured photopolymers (Liljenhjerte, Upadhyaya & Kumar, 2016), etc. Hyperelastic constitutive models assume that the strain energy density W of a material is a function of only the instantaneous deformation (or strain). Many empirical and semi-empirical forms of W are available in the literature. In the present study, two polynomial-based forms, the two-parameter Mooney-Rivlin (Mooney (1940); Rivlin (1948)) and the three-parameter generalized Rivlin models, and two exponential/logarithmic models, the Gent (Gent, 1996) and the Gent-Gent (Pucci & Saccomandi, 2002) models, are investigated. While the former two polynomial forms are phenomenological models that accurately capture hyperelastic material response in small to moderate ranges of strain (Marckmann and Verron (2006); Tobajas, Ibartz and Gracia (2016)), the latter two exponential/logarithmic models are motivated by molecular theory (non-Gaussian) and capture certain phenomena not

effectively modeled by the classical polynomial models (Horgan & Saccomandi, 2003) (e.g., limiting chain extensibility). All four of these models assume material isotropy and incompressibility, which are reasonable assumptions for these 3D networked materials that are predominantly composed of water (Baumberger, Caroli & Martina, 2006; Oyen, 2014). Specifically, for agarose gel, incompressibility (as Poisson's ratio of approximately 0.5) was confirmed experimentally by Normand et al. (Normand et al., 2000) and Subhash et al. (Subhash et al., 2011). The exact forms of these models are given as

$$W_{\rm MR} = A_{10}(I_1 - 3) + A_{01}(I_2 - 3) \tag{1a}$$

$$W_{GR} = A_{10}(I_1 - 3) + A_{01}(I_2 - 3) + A_{11}(I_1 - 3)(I_2 - 3)$$
(1b)

$$W_{\rm G} = -\frac{\mu J_m}{2} \ln \left(1 - \frac{I_1 - 3}{I_m} \right) \tag{1c}$$

$$W_{GG} = -\frac{\mu J_m}{2} \ln \left(1 - \frac{I_1 - 3}{J_m} \right) + \frac{3C_2}{2} \ln \left(\frac{I_2}{3} \right)$$
 (1d)

where subscripts MR, GR, G and GG denote the Mooney-Rivlin, generalized Rivlin, Gent and Gent-Gent models, respectively; A_{10} , A_{01} , A_{11} , μ , J_m and C_2 are model parameters. Note, J_m is the limiting chain extensibility parameter, which is a constant limiting value of I_1 – 3, such that $[W]_{(I_1-3)\to J_m}\to\infty$ (Horgan & Saccomandi, 2003). I_1 and I_2 are the principal invariants of the right Cauchy-Green deformation tensor \mathbf{C} ,

$$I_1 = \text{tr}(\mathbf{C}) = \lambda_1^2 + \lambda_2^2 + \lambda_3^2, \ I_2 = \frac{1}{2} \left[(\text{tr}\mathbf{C})^2 - \text{tr}(\mathbf{C}^2) \right] = \lambda_1^2 \lambda_2^2 + \lambda_2^2 \lambda_3^2 + \lambda_3^2 \lambda_1^2$$
 (2)

where λ_1 , λ_2 and λ_3 are the principal stretches (standard basis $\{{\bf e}_1, {\bf e}_2, {\bf e}_3\}$). Imposing the incompressibility constraint, $\det({\bf F}) = \lambda_1 \ \lambda_2 \ \lambda_3 = 1$, where ${\bf F}$ is the deformation gradient tensor (this condition has been experimentally validated from axial ($\lambda_2 = \lambda$) and transverse ($\lambda_1 = \lambda_3$, assuming isotropy) DIC stretch measurements in tensile test, as shown in the supplementary material). Regardless of the exact form of the strain energy density function, the nominal stress tensor ${\bf T}^0$ is given as

$$\mathbf{T}^{0^{\mathrm{T}}} = 2\mathbf{F} \cdot \frac{\partial W}{\partial \mathbf{C}} \tag{3}$$

Specifically, for the three primary deformation modes investigated in this study, the model stress-strain relations are

Compression and tension:
$$T_{11}^0 = 2 \frac{\partial W}{\partial I_1} \left(\lambda - \frac{1}{\lambda^2} \right) + 2 \frac{\partial W}{\partial I_2} \left(1 - \frac{1}{\lambda^3} \right)$$
 (4a)

Simple shear:
$$T_{21}^0 = 2\left(\frac{\partial W}{\partial I_1} + \frac{\partial W}{\partial I_2}\right)\gamma$$
 (4b)

where λ is the axial principal stretch in uniaxial deformation ($\lambda = 1 + \varepsilon$; ε is the axial nominal strain), and γ is the nominal shear strain. Eqs. (4a) and (4b) are used to fit the various hyperelastic models (Eq. (1)) to the experimentally obtained stress-strain data using least squares optimization. A detailed description of the fitting procedure and error analysis is given in the Appendix.

3.2. Computational finite element analysis

The hyperelastic constitutive modeling described in the previous subsection and the associated fitting procedure (Appendix) employ experimental data from the three primary homogeneous deformation modes of compression, tension and shear. To study and compare with experiments the outcome of these models in a non-homogeneous deformation mode, finite element (FE) simulation of the wedge indentation test is conducted using the commercial Abaqus/Standard 2017 software (Dassault Systèmes, France). Fig. 3 shows the FE model of agarose gel with a typical displacement-field map of the deformed mesh at 2 mm indentation. While the indenter is modeled as an analytical rigid surface, the gel sample is modeled using 8-node linear hexahedral elements with reduced integration and hybrid formulation (C3D8RH). Double biased seeding is implemented to ensure fine mesh near the indenter tip while optimizing computation time. A total of 20,102 elements and 22,560 nodes are created. Boundary conditions are set such that the bottom face of the gel sample is grounded ($u_2 = u_{R1} = u_{R3} = 0$), and a vertical displacement of $u_2 = -2$ mm is applied to the indenter (all other degrees of freedom are restricted). A frictionless general (standard) contact is implemented. Supplementary simulations for an FE mesh convergence study show that refining the mesh size further causes very little impact on the results.

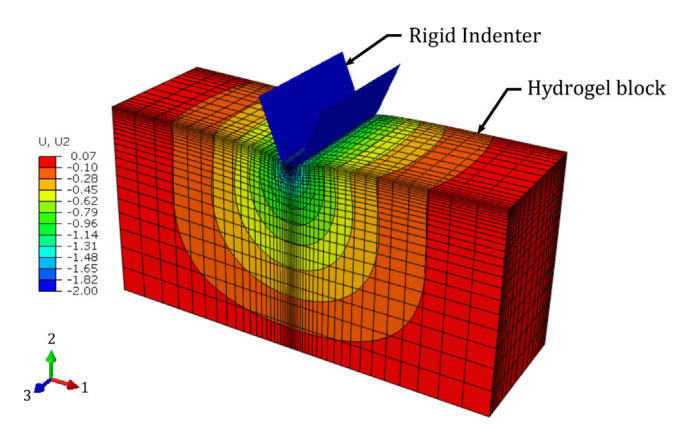


Fig. 3. FE model of the wedge indentation on a hydrogel block showing the deformed mesh and vertical displacement contours at 2 mm indentation depth (Units in legend: mm). (For interpretation of the references to color in this figure legend, the reader is referred to the web version of this article.)

4. Results and discussion

In the first subsection, the effect of agarose gel concentration on the molecular structure of the network is assessed using the experimentally measured modulus-concentration relation. The network structure dictates the macroscopic elastic behavior of a gel, and in turn the applicability of hyperelasticity in modeling such a response. Next, large deformation behavior under the three primary deformation modes is discussed, which is modeled using the hyperelastic models discussed in Section 3. The best model is implemented into FE simulations and is used to model the deformation state during wedge indentation. Model response and experimental results are then compared. Finally, the importance of considering multiple deformation modes in hyperelastic modeling is discussed.

4.1. Small strain elasticity and the range of entropic elastic behavior

The mechanical response of a hydrogel depends on the initial properties of the polymer-solvent mixture (average molecular weight of the polymer chains, gel concentration, temperature, etc.) and the resulting structural parameters of the gel (mesh size, stiffness and thickness of fibrils, crosslink functionality, etc.). For example, previous studies on agarose gel (Fujii, Yano, Kumagai & Miyawaki, 2000; Tokita & Hikichi, 1987) found that near the critical sol-gel transition concentration of ~0.071 wt.%, the modulus (G) scales with concentration (C) as a power law with exponent of 2.31, i.e. $G \sim c^{2.31}$. Normand et al. (Normand et al., 2000) showed that this scaling exponent decreases with concentration consistent with the Cascade theory (Clark & Ross-Murphy, 1985), which suggests that the number of elastically active network chains (EANCs) increases and the concentration of loose chains (dangling chains plus free chains) decreases with increasing gel concentration. Several studies (Ramzi, Rochas & Guenet, 1998; Rochas, Brûlet & Guenet, 1994) have suggested that as agarose gel consists of stiff rod-like fibrils (confirmed separately by small angle X-ray scattering (Ramzi et al., 1998) and electron microscopy (Dormoy & Candau, 1991) experiments), this scaling behavior can be studied using the Jones and Marques theory of rigid polymer networks (Jones & Marques, 1990). This theory suggests that the mechanical response of a rigid network of rod-like fibrils (fractal dimension, $D_f \approx 1$) follows enthalpic and entropic elasticity at low and high concentration regimes, respectively, such that the scaling laws in these two regimes are

$$E \sim \begin{cases} c^2, & c \le c_c \text{ (enthalpic)} \\ c^{1.5}, & c > c_c \text{ (entropic)} \end{cases}$$
 (5)

where E is the elastic (initial) modulus and c_c is the cross-over concentration between the two elasticity mechanisms.

Fig. 4(a) shows the initial modulus versus concentration (log-log) obtained from uniaxial compression experiments on agarose gels in the 0.4–4% w/v concentration range. The observed behavior agrees with existing literature in that the modulus-concentration scaling exponent (slope of the log-log plot) decreases with concentration (Clark, 1994; Normand et al., 2000). Furthermore, the observed behavior is also consistent with the Jones and Marques theory, suggesting different elasticity mechanisms in the low and high gel concentration regimes. Considering only the concentration range of 1.5–4% w/v, a scaling exponent of 1.5 is obtained, which points to an entropic elastic response according to the Jones-Marques theory (Eq. (5)). Ramzi et al. (Ramzi et al., 1998) also reached this conclusion via dynamic (oscillatory) compression experiments. The same scaling response (exponent of 1.5) in this concentration range is also observed for the other two primary deformation modes of tension (Fig. 4(b)) and shear (Fig. 4(c)). Microstructurally in this high concentration range, the network junctions of agarose gel become flexible, and thus any external force tends to change the conformation of the network, giving rise to entropic elasticity.

Figures (4a) and (4b) also include results from a number of other studies in compression (Normand et al., 2000; Subhash et al., 2011; Zhang & Rochas, 1990) and tension (Kwon et al., 2010; Normand et al., 2000; Subhash et al., 2011). Not

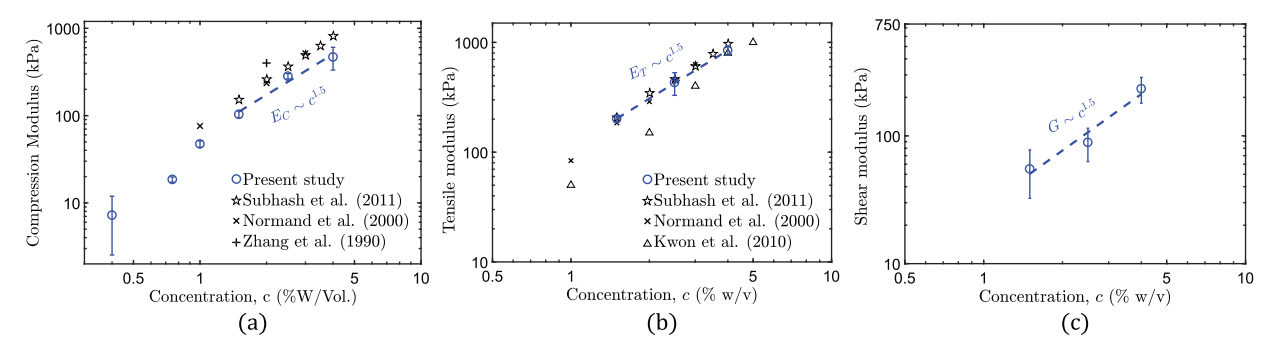


Fig. 4. Elastic modulus versus gel concentration for agarose gel under (a) uniaxial compression, (b) uniaxial tension, and (c) simple shear.

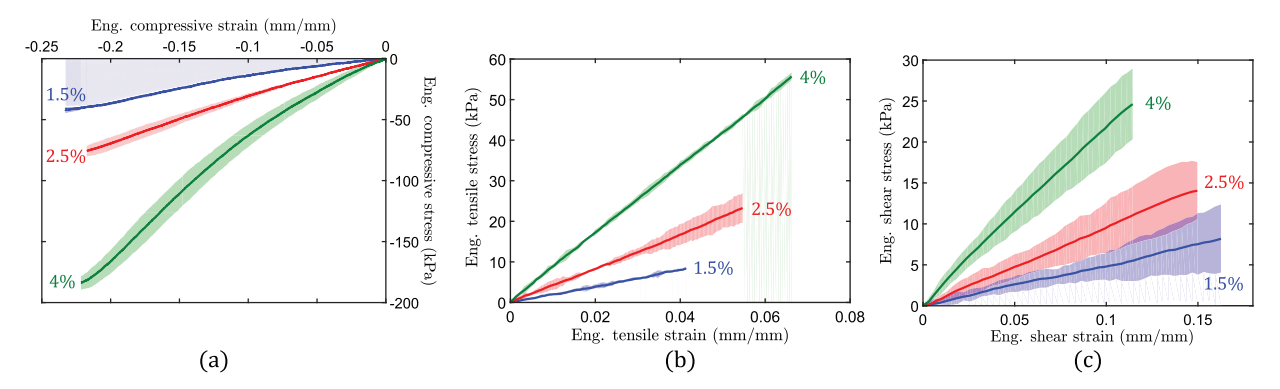


Fig. 5. Engineering stress versus strain plots of high concentration (>1.5%) agarose specimens in (a) uniaxial compression, (c) uniaxial tension, and (e) simple shear.

including oscillatory shear experiments, to the author's knowledge, the present study is the first to experimentally study single pulse simple shear response of agarose gel (both small and large deformation). Notice that the exact values of modulus from different literature sources do not match, which is not surprising owing to the possible differences in chemical (e.g., average molecular weight, solvent ionic strength) and physical (e.g., strain rate) conditions leading to the mechanical tests. Of importance is the scaling exponent between the modulus and gel concentration, which is approximately 1.5 across the included experimental data in 1.5–4% w/v concentration range, pointing to an ideal entropic hyperelastic behavior (tension data by Kwon et al. (Kwon et al., 2010) is an exception with a scaling exponent of ~2.1). Overall, as hyperelasticity (or rubber elasticity) assumes a purely entropic deformation (zero energy dissipation), the present study considers only the latter high concentration regime (1.5–4% w/v) for large deformation analysis.

4.2. Large deformation behavior in primary deformation modes

Agarose gels of concentrations 1.5, 2.5 and 4% w/v (entropic elasticity range) are tested in all three primary deformation modes to provide data necessary for a model of their hyperelastic response. Figs. 5(a), 5(b) and 5(c) show the stress-strain plots for uniaxial compression, uniaxial tension and simple shear deformations, respectively. Note, compressive stress versus strain is plotted in the third quadrant, with the engineering stress and strain on the negative ordinate and abscissa, respectively. The shaded region around individual plots represents the t-test 95% confidence interval.

Both elastic modulus and stress to failure increase with increasing gel concentration, which is caused by the increasing number of EANCs (and so the crosslink density) as the network mesh size decreases. Under uniaxial deformation, the average compressive failure stress at any gel concentration is ~3–4 times the average tensile failure stress. In contrast, the average tension modulus is greater than the corresponding average compression modulus for every gel concentration. Out of the three deformations, compression exhibits the most nonlinear behavior.

The shear stress-strain data shows a greater amount of variation as compared to the compression and tension test results. This variation is possibly a result of handling difficulties with thin shear specimens (thickness ~10 times smaller than the shortest dimension of tensile or compressive specimens), which include gluing the specimen between shear plates and transferring this setup onto the test fixture, which may cause some surface damage in the gel specimen and/or uneven adhesion with the shear plates. Regardless, a clear separation in the shear stress-strain plot is apparent between the three agarose gel concentrations studied.

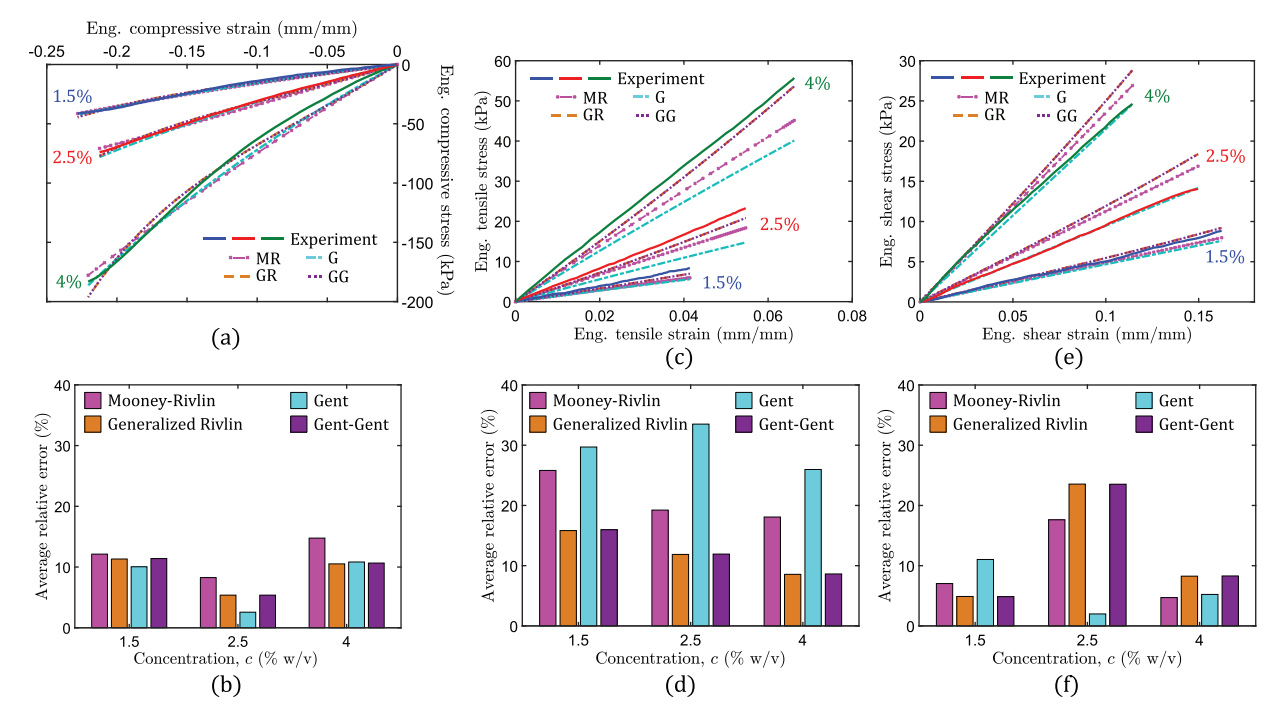


Fig. 6. Experimental and model fitted (using Mooney-Rivlin, generalized Rivlin, Gent and Gent-Gent models) engineering stress versus strain plots of high concentration (>1.5%) agarose specimens in (a) uniaxial compression, (c) uniaxial tension, and (e) simple shear. Average relative residual error (%) versus gel concentration (% w/v) resulting from the four hyperelastic models in (b) uniaxial compression, (d) uniaxial tension, and (f) simple shear. (For interpretation of the references to color in this figure legend, the reader is referred to the web version of this article.)

Table 1Model parameters and overall average residual error of fit resulting from the application of four hyperelastic models (Eq. (1)) to experimental data for three gel concentrations.

Gel conc. (% w/v)	Mooney-Rivlin (kPa)			Generalized Rivlin (kPa)				Gent (kPa)			Gent-Gent (kPa)			
	$\overline{A_{10}}$	A ₀₁	err (%)	$\overline{A_{10}}$	A ₀₁	A ₁₁	<u>err</u> (%)	$\overline{\mu}$	J _m	err (%)	$\overline{\mu}$	J_m	C ₂	<u>err</u> (%)
1.5	30.48	-5.89	14.99	83.14	-56.43	31.39	10.68	46.79	4.76E6	16.93	164.01	1.84	-110.64	10.74
2.5	106.26	-49.89	15.04	203.47	-145.26	71.26	13.60	94.71	4.21E7	12.69	405.34	2.09	-288.98	13.61
4	170.83	-53.16	12.52	415.17	-293.74	175.62	9.11	215.04	9.39E6	14.01	819.67	1.60	-576.73	9.20

4.3. Hyperelastic constitutive modeling

Figs. 6(a), 6(c) and 6(e) show the numerically fitted stress-strain plots using the four hyperelastic models (Mooney-Rivlin (MR), generalized Rivlin (GR), Gent (G), and Gent-Gent (GG)) in compression, tension and shear deformations, respectively. Figs. 6(b), 6(d) and 6(f) show the corresponding average residual errors of fit for individual deformation modes for each gel concentration, as calculated using Eq. (14) (see Appendix). The exact values of model parameters for each gel concentration and associated residual errors (averaged over the three deformation modes) are given in Table 1.

Not including the Gent model, which consistently yields poor accuracy in tension ($\overline{\text{err}} > 25\%$), all other hyperelastic models provide a reasonable agreement with the experimental data for each gel concentration. In addition, although the Gent model gives accurate values of T_{21}^0 in simple shear, it was shown by Puglisi and Saccomandi (Puglisi & Saccomandi, 2016) that it gives unrealistic values for the normal stresses in this deformation mode, limiting its applicability in three-dimensional stress state modeling. In fact, dependence of the strain energy density on both principal invariants (I_1 and I_2) has recently been demonstrated to be a fundamental requirement for incompressible rubber-like materials (Destrade, Saccomandi & Sgura, 2017). Further, in the absence of a clear limiting chain extensibility response (i.e., stress tending to infinity on approaching a particular strain value (Horgan & Saccomandi, 2003)), the J_m values obtained numerically in the Gent model are unreasonably large and do not show any trend against gel concentration (see Table 1). The latter fact is also true for the Gent-Gent model, which otherwise shows excellent agreement with the experimental data. On the other hand, the polynomial generalized Rivlin model provides almost the same accuracy (slightly lower average residual error) as the Gent-Gent model with equal number of model parameters, and at same time prevents possible computational problems inherent to the calibration of logarithmic/exponential models in which model parameters occur nonlinearly in stress-deformation equations (e.g., non-unique optimal solutions and issues related to the choice of initial guess in nonlinear curve fitting).

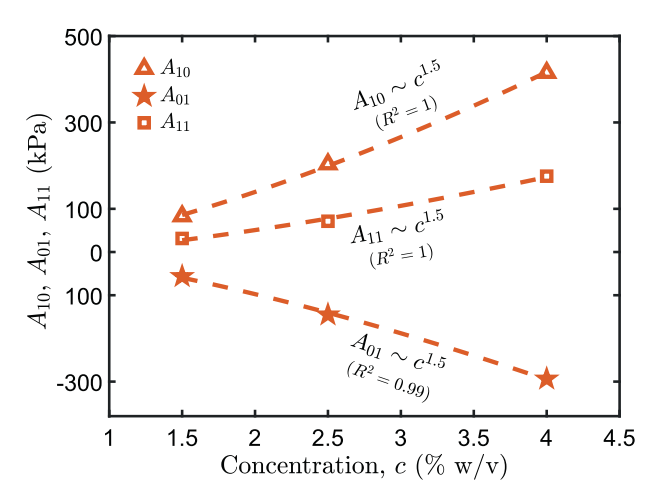


Fig. 7. Evolution of the generalized Rivlin model parameters with agarose gel concentration (% w/v) in the high concentration entropic elasticity regime.

In addition, unlike the Gent-Gent model, this model (as polynomial strain energy density functions) is available in most commercial finite element software, thus leading to its convenient implementation to study 3D loading applications. Clearly, the Gent-Gent model, which provides superior fitting in the case of hyperelastic materials that exhibit extreme deformations (Destrade et al., 2017), does not lead to any improvement in fitting accuracy in the case of agarose gels, while the three-parameter generalized Rivlin model provides additional benefits.

The variation of model parameters of the generalized Rivlin model with gel concentration can be described using a positive curvature power law trend with an exponent of 1.5,

$$A_{10}(c) = -12.76 + 53.67c^{1.5} (6a)$$

$$A_{01}(c) = 10.75 - 38.27c^{1.5} (6b)$$

$$A_{11}(c) = -16.27 + 23.72c^{1.5}$$
 (6c)

where the model parameters are in kPa and gel concentration is in % w/v. The power-law variation of generalized Rivlin model parameters versus agarose gel concentration (Eq. (6)) is plotted in Fig. 7. As the initial modulus of the generalized Rivlin model is given by $G_0 = 2(A_{10} + A_{01})$, the scaling behavior of model elastic modulus in the small strain regime is consistent with both the experimental findings (Figs. 5(b), 5(d) and 5(f)) and the Jones and Marques theory (Eq. (5)),

$$G_0 = -4.02 + 30.8c^{1.5} \tag{7}$$

where G_0 is in kPa. Such a clear and consistent trend in model parameters is not present in the Mooney-Rivlin model, where a negative curvature power law trend of model parameters versus gel concentration is obtained (A_{10} , $A_{01} \sim c^n$, n < 1). Therefore, superior fitting accuracy and a definitive trend of model parameters versus gel concentration that is consistent with established scaling relations makes the generalized Rivlin model best suited for modeling the mechanical response of agarose gel in all primary deformation modes.

Using Eq. (6) for model parameters, the generalized Rivlin strain energy density function (Eq. (1b)) for agarose gel is constructed. The so obtained Extended Generalized Rivlin (EGR) Model is

$$W_{\text{EGR}} = [A_{10}(c)](I_1 - 3) + [A_{01}(c)](I_2 - 3) + [A_{11}(c)](I_1 - 3)(I_2 - 3), \ c \ (\% \ \text{w/v}) \ \epsilon \ [1.5, \ 4]$$
(8)

where W_{EGR} is the strain energy density in kPa, and $A_{10}(c)$, $A_{01}(c)$ and $A_{11}(c)$ are polymer concentration dependent model parameter functions (kPa units) as given in Eq. (6). Further, as the network mesh size (ξ) is directly related to the gel concentration using scaling laws (Stauffer, Coniglio & Adam, 1982), any model that relates concentration to mechanical properties also relates mesh size to the latter. For agarose gel, the following relation was obtained by Righetti et al. (Righetti, Brost & Snyder, 1981) using electrophoresis measurements on latex spheres

$$\xi = 140.7c^{-0.7} \tag{9}$$

where the network mesh size ξ is in nm. Using Eqs. (6), (8) and (9), the *Extended Generalized Rivlin Model* is given in terms of the microstructural parameter of average mesh (or pore) size as

$$W_{\text{EGR}} = [\psi_{10}(\xi)](I_1 - 3) + [\psi_{01}(\xi)](I_2 - 3) + [\psi_{11}(\xi)](I_1 - 3)(I_2 - 3), \ \xi(nm) \ \epsilon \ [50, \ 106]$$

$$\tag{10}$$

where

$$\psi_{10}(\xi) = -12.76 + (2.154 \times 10^6)\xi^{-2.15} \tag{11a}$$

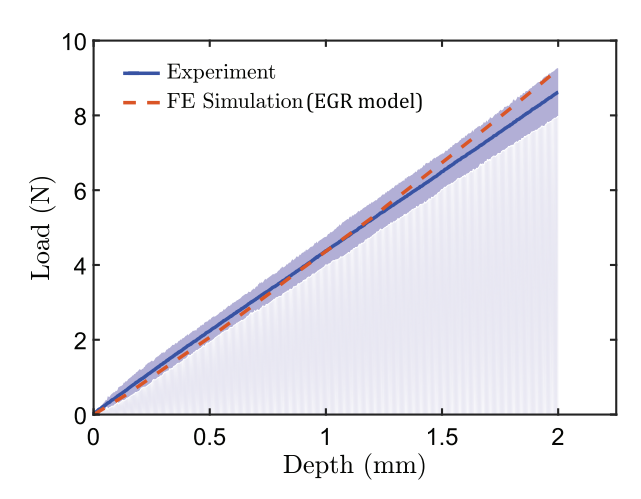


Fig. 8. Wedge indentation load versus depth plot of 3% w/v agarose gel as obtained from experiments and FE simulations using the extended generalized Rivlin (EGR) model.

$$\psi_{01}(\xi) = 10.75 - (1.536 \times 10^6)\xi^{-2.15} \tag{11b}$$

$$\psi_{11}(\xi) = -16.27 + (9.519 \times 10^5)\xi^{-2.15}$$
(11c)

The concentration dependent extended generalized Rivlin model (Eq. (8)) will now be implemented in finite element (FE) analysis to predict the mechanical response of 3% w/v agarose hydrogel under wedge indentation, which is a complex three-dimensional strain state with non-zero normal and shear components. This will help evaluate not only the veracity of this model for concentrations other than those initially used for its calibration (1.5, 2.5 and 4% w/v), but also its transferability to model a non-homogeneous and triaxial stress state.

4.4. Application of the "Extended" generalized rivlin model to wedge indentation response

From Eq. (6), the extended generalized Rivlin model parameters for 3% w/v agarose gel are obtained as $A_{10} = 266.12$ kPa, $A_{01} = -188.11$ kPa and $A_{11} = 106.98$ kPa. These parameters are used to define the hyperelastic agarose gel material in FE simulation of wedge indentation (Section 3.2) via the built-in "polynomial" strain energy potential of order 2 in Abaqus/Standard (Abaqus v6.12 Analysis User's Manual, 2012). Fig. 8 shows the load-depth response obtained from experiments and FE simulation. The shaded area in the experimental response represents the *t*-test 95% confidence interval.

The extended generalized Rivlin model shows an excellent agreement with the experimental response throughout the investigated range of depth. The average relative error with respect to the mean experimental values is 5.32% (max. relative error ~11%).

Next, the surface strain distributions obtained from experiments (via DIC) and FE simulations in a rectangular area of interest (40 mm x 23.5 mm) for a fixed load value are compared. This load value is taken as 8.62 N, which is the average load corresponding to the maximum indenter depth of 2 mm in experiments. Fig. 9 compares the various full-field engineering strain maps of 3% w/v agarose gel: (a) ε_{11} (xx component), (b) ε_{22} (yy component), (c) ε_{12} (in-plane shear component), and (d) ε_{33} (out-of-plane zz component). Identical color map ranges are used for both DIC and FE strain fields of individual strain components. The black and gray regions in the FE contour maps correspond to fast-varying strains concentrated near the indenter tip. As DIC measurements report averaged strain values over a certain area dependent on subset and step sizes (further smoothed using a strain filter), these extreme strains lie outside the range of DIC color maps.

A very good agreement is observed between DIC and FE strain components both in terms of the qualitative shape of the field and the actual quantitative values. This exercise shows that the extended generalized Rivlin model is applicable not only to simple primary homogeneous deformation modes, but also to more complex triaxial deformations in the investigated range of gel concentrations.

4.5. Importance of multi-deformation mode consideration in hyperelastic constitutive modeling

Empirical recommendations and recent thermodynamic stability analyses have suggested consideration of multiple deformation modes for calibrating hyperelastic models (Ogden, Saccomandi, & Sgura, 2004; Upadhyay, Subhash, & Spearot, 2019b); . Nonetheless, numerous mechanical characterization studies consider only a single deformation mode for modeling purposes, which limits their predictive capability to only that particular deformation mode. In this section, the consequence

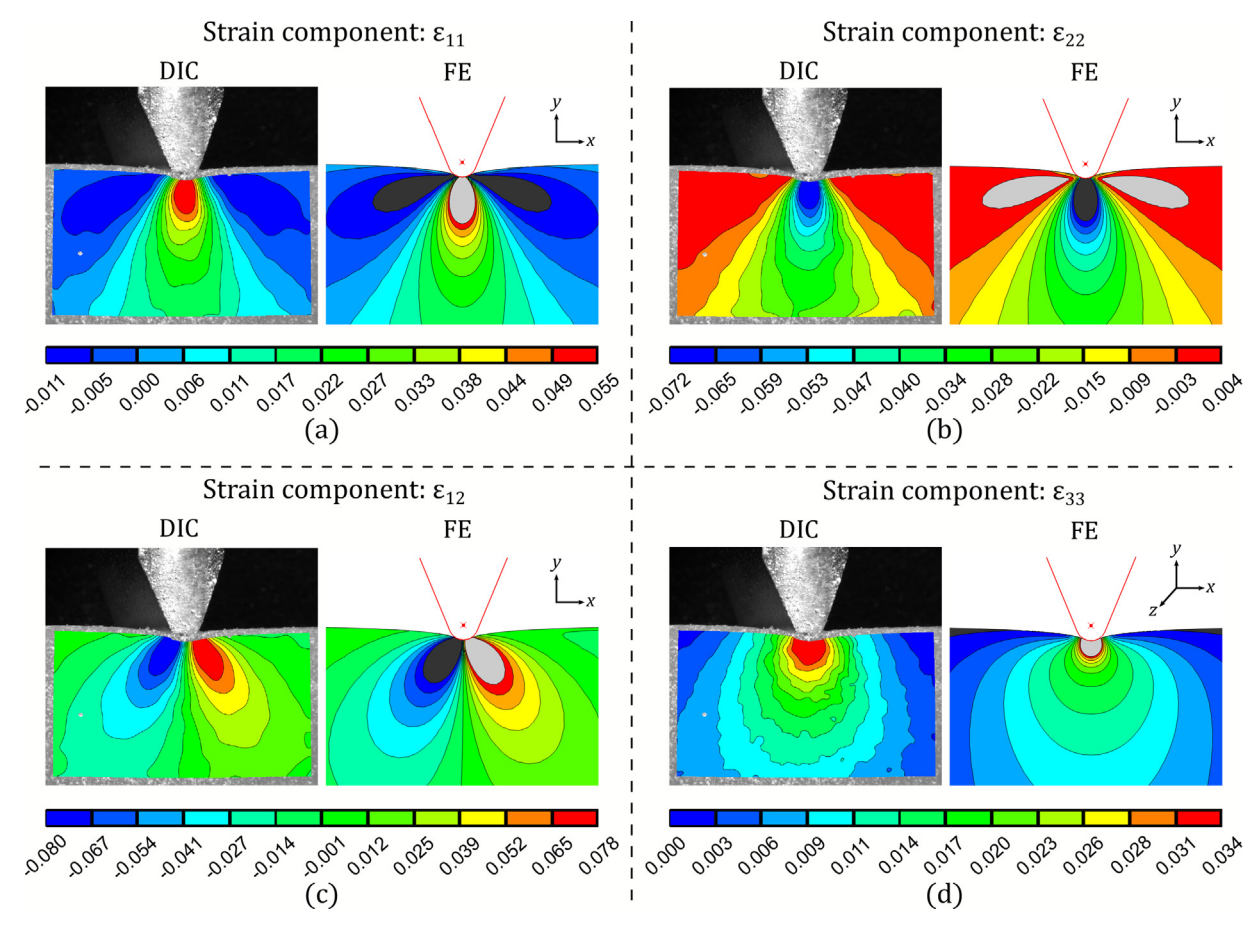


Fig. 9. Comparison of strain-fields as obtained from experiments (via DIC) and FE simulations in the area of interest (40 mm x 23.5 mm): (a) ε_{11} (xx), (b) ε_{22} (yy), (c) ε_{12} (xy), and (d) ε_{33} (zz) engineering strain components. (For interpretation of the references to color in this figure legend, the reader is referred to the web version of this article.)

of considering fewer deformation modes in hyperelastic modeling on the overall fitting accuracy under various deformations is studied. Four cases are considered: only compression data, only tension data, combined compression and tension data, and data from all primary deformation modes (compression, tension and shear). Note that the shear only case results in an indeterminate solution for model constants A_{10} and A_{01} (see Eq. 4(b)) and thus cannot be used alone in the calibration of the Mooney-Rivlin and the generalized Rivlin models. The generalized Rivlin model parameters obtained in the four cases and the resulting average residual errors over the three gel concentrations in different primary deformation modes (compression (C), tension (T), and shear (S)) are given in Table 2.

From Table 2, when only the compression data is used to calibrate the generalized Rivlin model, the resulting model yields a very low average residual error ($\overline{\textbf{err}}$ (%) = 1.56%) in compression. However, large errors are obtained for the other two homogeneous deformations of tension (53.65%) and shear (30.28%). Similarly, the generalized Rivlin model calibrated using only tension data results in a very good accuracy in tension ($\overline{\textbf{err}}$ (%) = 1.02%), but a poor accuracy in other two deformations. On the other hand, when multiple deformation modes are simultaneously considered, the overall fitting accuracy is considerably improved. Interestingly, modeling using the combined compression-tension data results in a good accuracy for shear deformation as well (deformation mode not considered in the initial calibration).

The superior fitting accuracy of hyperelastic models calibrated using multiple deformation modes is also observed for the three-dimensional stress state of wedge indentation. For example, Fig. 10 shows the experimentally obtained load versus depth response of 2.5% w/v agarose gel samples along with finite element predictions from generalized Rivlin models corresponding to the four cases of deformation mode consideration. Both combined compression-tension and combined compression-tension-shear cases result in load-depth predictions that agree very well with the experimental data. On the other hand, the compression only and tension only cases result in under- and over-predicted responses, with average residual errors of approximately 15% and 73%, respectively. Out of the two single deformation mode cases, the compression only case yields a relatively reasonable indentation load-depth response. This is likely due to the dominance of compressive strains/stresses in the region near the indenter tip (see Fig. 9).

Table 2Model parameters and overall average residual error of fit resulting from the generalized Rivlin hyperelastic model (Eq. (1b)) when different set of primary deformation modes are considered in the fitting procedure.

Deformation mode(s)		Generalized	Rivlin paramete	r (kPa)	err (%) over all concentrations			
considered	Gel conc. (% w/v)	$\overline{A_{10}}$	A_{01}	A ₁₁	С	T	S	
Compression only	1.5	-67.67	81.81	-32.44	1.56	53.65	30.28	
•	2.5	21.01	23.69	-15.15				
	4	-252.72	320.94	-120.03				
Tension only	1.5	17.17	15.28	343.74	232.94	1.02	49.82	
	2.5	-51.52	122.86	609.71				
	4	-176.02	327.73	744.29				
Compression + Tension	1.5	93.88	-66.26	35.89	10.11	8.10	16.27	
•	2.5	246.90	-184.83	89.22				
	4	430.61	-307.44	180.44				
Compression + Ten-	1.5	83.14	-56.43	31.39	9.07	12.09	12.23	
sion + Shear	2.5	203.47	-145.26	71.26				
	4	415.17	-293.74	175.62				

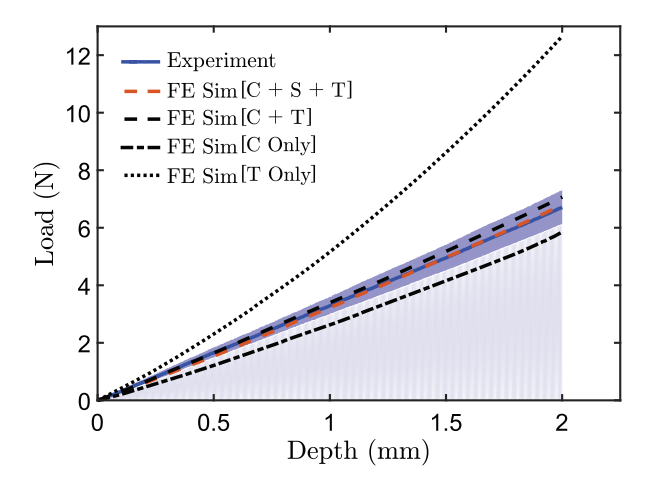


Fig. 10. Load versus depth plot for 2.5% w/v agarose gel as obtained from experiments and FE simulations. Four different cases of deformation mode considerations in calibrating generalized Rivlin model for FE simulations are evaluated. (For interpretation of the references to color in this figure legend, the reader is referred to the web version of this article.)

Further, unlike the model parameters obtained in single deformation mode cases, the three generalized Rivlin model parameters for different gel concentrations in the multiple deformation mode cases show consistency both in terms of their sign and monotonicity (with respect to gel concentration), as shown in Fig. 11. Comparing the two multi-deformation mode cases (Figs. 11(c) and 11(d)), the combined compression-tension-shear case provides lower average relative errors and scaling behavior among individual model parameters (A_{10} , A_{01} , $A_{11} \sim c^{1.5}$) that is consistent with small-strain elastic behavior and the Jones-Marques theory (Eq. (5); Section 3.1).

5. Summary and conclusion

Uniaxial compression, uniaxial tension, simple shear and wedge indentation experiments are conducted to study, model and validate the three-dimensional constitutive behavior of agarose hydrogels across a range of gel concentrations. Both small strain and large nonlinear deformation regimes are investigated.

Compression experiments are conducted on six different gel concentration samples (0.4, 0.75, 1, 1.5, 2.5 and 4% w/v). The variation of elastic modulus with gel concentration shows a power law exponent of ~1.5 in the high concentration (1.5, 2.5, 4% w/v) range. This observation confirms the existence of entropic elasticity (as per the Jones and Marques theory) in high concentration agarose gel, which was also identified by previous studies (Guenet & Rochas, 2006; Ramzi et al., 1998). The power law exponent of ~1.5 in this concentration range is also found in data from the other two primary deformation experiments of uniaxial tension and simple shear. As entropic elasticity is a fundamental assumption in hyperelasticity, only the 1.5–4% w/v range is considered for constitutive modeling.

Large deformation stress-strain data from the three primary deformation modes is modeled using four hyperelastic models, two of which are polynomial based (Mooney-Rivlin and three-parameter generalized Rivlin) and the other two are exponential/logarithmic (Gent and Gent-Gent). The Gent model results in a poor accuracy (high residual error) when fitting

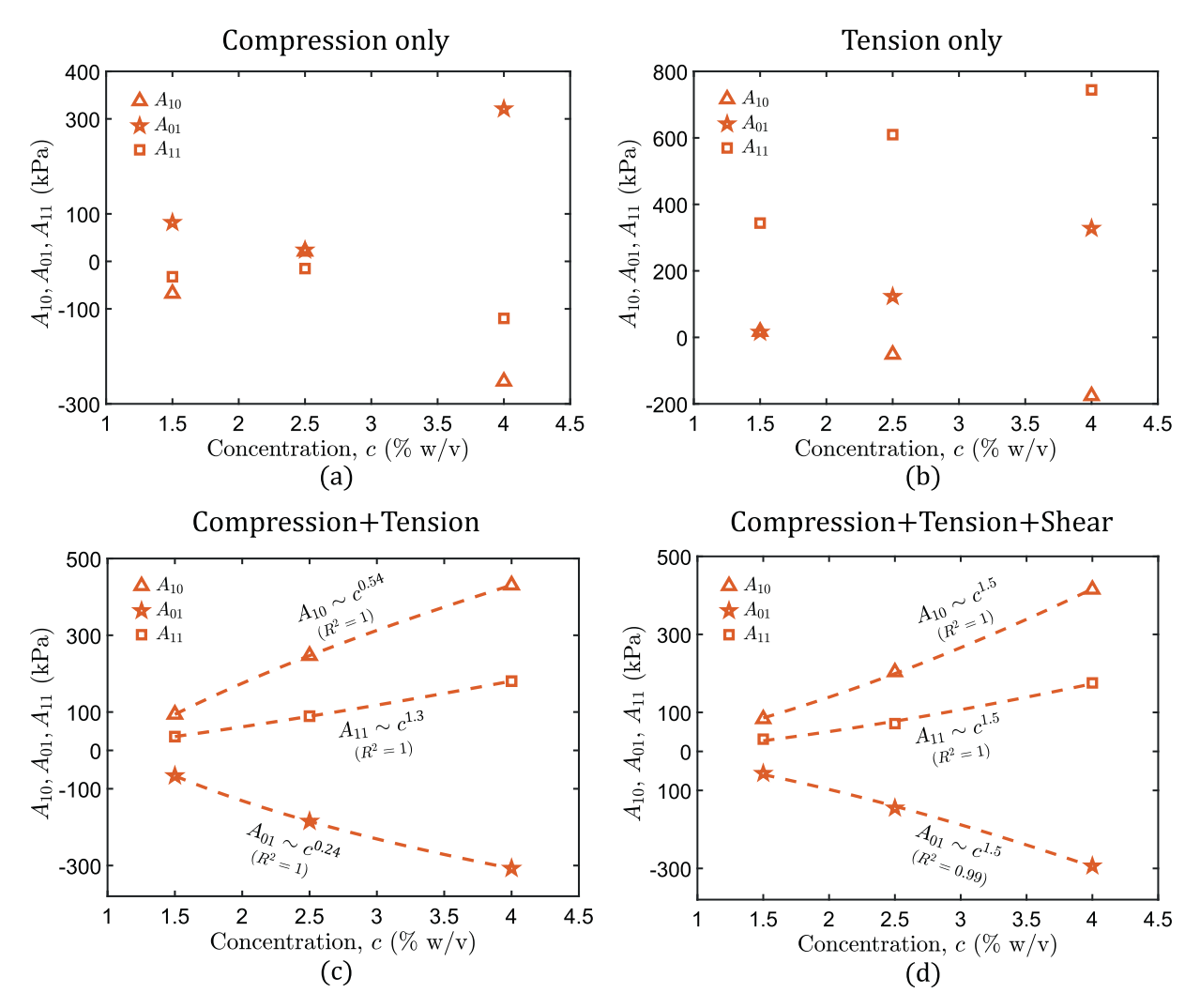


Fig. 11. Evolution of the three-parameter generalized Rivlin model parameters with agarose gel concentration ($c \in [1.5, 4]$) when different sets of deformation modes are considered in model calibration: (a) Only compression test data, (b) Only tension test data, (c) Combined compression-tension data, and (d) Combined compression-tension-shear data.

to tension data; all other models show reasonable agreement in all deformation modes and in every gel concentration. The J_2 parameter of the Gent and Gent-Gent models shows no correlation with gel concentration, which is attributed to the absence of a clear limiting chain extensibility behavior in the stress-strain data of agarose gel. It is concluded that as the agarose gel does not exhibit extreme stretches/strains, the polynomial-based models offer simple mathematical forms that prevent curve fitting optimization issues, are available in commercial FE software, and can capture the response with good accuracy. It is expected that other hydrogels that deform only in the small-moderate strain regime will also be satisfactorily modeled using the polynomial-based models. Among the Mooney-Rivlin (this is in fact equivalent to a first-order Taylor expansion of the Gent-Gent model) and the generalized Rivlin models, the latter leads to a superior fitting accuracy because of the added flexibility allowed by an additional model constant via dependence on higher order terms (as $(I_1 - 3)(I_2 - 3)$), and shows a remarkable trend in its model parameters versus gel concentration (or network mesh size) that is consistent with the scaling relations obtained in the small-strain regime. The so obtained extended generalized Rivlin model is a three-dimensional constitutive relation valid across a range of gel concentrations.

To validate the applicability of the extended generalized Rivlin model to an arbitrary concentration within the entropic regime and under a complex deformation, the model is employed in FE simulations of the non-homogeneous triaxial wedge indentation deformation of 3% w/v agarose hydrogel. The model prediction of load-depth response shows excellent agreement with experimental wedge indentation data. Furthermore, the strain-fields near the indenter tip for a particular load are also compared between model and experiments. A good agreement is observed for all the non-zero strain fields, i.e., the normal ε_{11} , ε_{22} , ε_{33} as well as in plane-shear ε_{12} components.

Finally, the consequence of using fewer deformation modes in the calibration of the three-parameter generalized Rivlin model is highlighted. Specifically, consideration of a single deformation mode (compression or tension) leads to poor fitting

accuracy in other primary deformation modes. However, when both compression and tension are combined, a reasonable prediction of both shear and triaxial indentation data is obtained. The overall residual errors are further reduced when the shear stress-strain data is added; this improvement is not as significant as when the second uniaxial deformation mode is added for model calibration. From a practical standpoint, this result is encouraging because stress-strain data under shear is often unavailable due to complexities in performing the experiment. Interestingly, the importance of considering both compression and tension deformations was also elucidated mathematically by Upadhyay et al. (Upadhyay et al., 2019b), who showed that these two deformations pose opposing restrictions on the bounds of the model constants of the Mooney-Rivlin and the generalized Rivlin models.

The experimental procedures outlined in this study can be used for most soft polymeric gels and biological tissues. However, the analytical procedure should be used with caution keeping in mind the underlying assumptions of hyperelasticity, which require the material to show a fully-reversible and entropic deformation. This may not be true at very low or high temperatures (Anseth et al., 1996), under variable loading rates (Upadhyay et al., 2020), etc. These situations promote dissipative or viscoelastic effects, which will be considered in future work to expand the applicability of the extended generalized Rivlin model. Finally, it is worth noting that hyperelastic models (where stress is a function of deformation gradient) are a subclass of a more general class of implicit constitutive models (Rajagopal, 2003, 2007) that consider a locus for the stress and kinematic variables, rather than explicitly defining one in terms of the other. A special type of such models are explicit formulations in which the deformation gradient is expressed as a function of stress. This new approach presents several advantages over traditional hyperelastic models and its recent application on modeling tensile response (both uniaxial and biaxial) of rubber has shown promising results (see (Muliana, Rajagopal, Tscharnuter, Schrittesser & Saccomandi, 2018)). Application of this approach to modeling 3D response of hydrogels presents another avenue for future research.

Acknowledgements

This work was supported by the National Science Foundation under grant nos. CMMI-1634188 and CMMI-1762791 to the University of Florida, Gainesville, USA.

Appendix. Model calibration using least squares optimization

The following least squares minimization problem is considered to fit Eqs. (4a) and (4b) to the test data

$$\min_{p} \sum_{i=1}^{N_{\text{exp}}} \sum_{i=1}^{m} \left[f_{i}^{j} \left(\Lambda_{i}^{j}, \mathbf{p} \right) - \tau_{i}^{j^{0, \text{exp}}} \right]^{2} \tag{12}$$

where $\mathbf{p} = [p_1, p_2, \dots, p_n]^{\mathrm{T}}$ is the vector containing model parameters (n total); Λ_i^j and $\tau_i^{j^{0,exp}}$ are the i^{th} experimental strain and stress values, respectively, in j^{th} deformation mode (compression, tension and shear), m is the total number of data points (Λ_i , $\tau_i^{0,exp}$) per deformation mode, N_{exp} is the number of deformation modes tested (three in the present study), and $f_i^j(\Lambda_i^j,\mathbf{p})$ is the symbolic nominal stress expression formulated using some hyperelastic model (e.g., Eqs. (4a) and (4b)). Note, Λ is a generic strain measure that represents stretch (λ) in a uniaxial compression/tension experiment and shear strain (γ) in a simple shear experiment.

For polynomial-based models (Eqs. (1a) and (1b)), the function $f(\Lambda, p)$ is linear in p and the coefficient matrix $A(f(\Lambda, p) = A(\Lambda) \cdot p)$ is full rank; thus, Eq. (12) results in a unique set of model parameters using the linear least squares technique (Ogden et al., 2004). Logarithmic Gent and Gent-Gent models, however, result in a function $f(\Lambda, p)$ that is nonlinear with respect to p; thus, a nonlinear least squares solution is required. In these cases, the *Lsqcurvefit* function of MATLAB is used with the trust-region-reflective (TR) method (Coleman & Li, 1996). The necessary conditions for thermodynamic stability of individual models (Upadhyay et al., 2019b) are used to provide bounds for the solution search. The convergence criterion is set such that the algorithm stops when either the Newton step becomes smaller than 10^{-8} , the supremum norm of the objective function gradient becomes less than 10^{-12} , or the number of iterations surpasses 3000. Finally, the relative errors are calculated for each hyperelastic model as

$$\operatorname{err}_{i}^{j} = \frac{\left| f_{i}^{j}(\Lambda_{i}^{j}, \mathbf{p}^{*}) - \tau_{i}^{j0, \exp} \right|}{\max\left\{ 0.1 \max\left(\tau_{i}^{j0, \exp}\right), \tau_{i}^{j0, \exp} \right\}}, \quad i = 1, 2, \dots, m; \quad j = 1, 2, \dots, N_{exp}$$

$$(13)$$

where p^* represents the vector containing optimal model parameters. Note that the term $(0.1 \text{max}(\tau^{0.\text{ exp}}))$ is added in the denominator to avoid division by very small stresses in the small strain regime, which otherwise would result in falla-

ciously large error values. Average percentage relative errors ($\overline{\text{err}}(\%)$) are reported as the measure of the goodness of fit. For a particular deformation mode (fixed i),

$$\overline{\operatorname{err}}^{j}(\%) = \frac{100}{m} \times \sum_{i=1}^{m} \operatorname{err}_{i}^{j} \tag{14}$$

References

Abaqus v6.12 Analysis User's Manual. (2012). Dassault Systemes Simulia Corp.

Agnelli, S., Baldi, F., Bignotti, F., Salvadori, A., & Peroni, I. (2018). Fracture characterization of hyperelastic polyacrylamide hydrogels. *Engineering Fracture Mechanics*, 203(June), 54–65. doi:10.1016/j.engfracmech.2018.06.004.

Anseth, K. S., Bowman, C. N., & Brannon-Peppas, L. (1996). Mechanical properties of hydrogels and their experimental determination. *Biomaterials*, 17(17), 1647–1657. doi:10.1016/0142-9612(96)87644-7.

Baumberger, T., Caroli, C., & Martina, D. (2006). Solvent control of crack dynamics in a reversible hydrogel. Nature Materials, 5(7), 552-555. doi:10.1038/nmat/1666.

Buckley, C. T., Thorpe, S. D., O'Brien, F. J., Robinson, A. J., & Kelly, D. J. (2009). The effect of concentration, thermal history and cell seeding density on the initial mechanical properties of agarose hydrogels. *Journal of the Mechanical Behavior of Biomedical Materials*, 2(5), 512–521. doi:10.1016/j.jmbbm.2008. 12.007.

Budday, S., Sommer, G., Birkl, C., Langkammer, C., Haybaeck, J., & Kohnert, J. (2017). Mechanical characterization of human brain tissue. *Acta Biomaterialia*, 48, 319–340. doi:10.1016/j.actbio.2016.10.036.

Castilho, M., Hochleitner, G., Wilson, W., van Rietbergen, B., Dalton, P. D., & Groll, J. (2018). Mechanical behavior of a soft hydrogel reinforced with three-dimensional printed microfibre scaffolds. *Scientific Reports*, 8(1), 1245. doi:10.1038/s41598-018-19502-y.

Chen, Q., Suki, B., & An, K.-. N. (2004a). Dynamic mechanical properties of agarose gels modeled by a fractional derivative model. *Journal of Biomechanical Engineering*, 126(5), 666. doi:10.1115/1.1797991.

Chen, W. W. (2016). Experimental methods for characterizing dynamic response of soft materials. *Journal of Dynamic Behavior of Materials*, 2(1), 2–14. doi:10.1007/s40870-016-0047-5.

Chen, Z.-. J., Gillies, G. T., Broaddus, W. C., Prabhu, S. S., Fillmore, H., & Mitchell, R. M., Corwin, F. D., & (2004b). A realistic brain tissue phantom for intraparenchymal infusion studies. *Journal of Neurosurgery*, 101(2), 314–322. doi:10.3171/jns.2004.101.2.0314.

Clark, A. H. (1994). Rationalisation of the elastic modulus-molecular weight relationship for kappa-carrageenan gels using cascade theory. Carbohydrate Polymers, 23(4), 247–251. doi:10.1016/0144-8617(94)90186-4.

Clark, Allan H., & Ross-Murphy, S. B. (1985). The concentration dependence of biopolymer gel modulus. British Polymer Journal, 17(2), 164–168. doi:10.1002/pi.4980170214.

Clark, Allan H., & Ross-Murphy, S. B. (1987). Structural and mechanical properties of biopolymer gels. In *in* Biopolymers (pp. 57–192). Springer-Verlag.

doi:10.1007/6Fb0023332.
Coleman, T. F., & Li, Y. (1996). An Interior trust region approach for nonlinear minimization subject to bounds. SIAM Journal on Optimization, 6(2), 418–445. doi:10.1137/0806023.

Deepthi, R., Bhargavi, R., Jagadeesh, K., Vijaya, M. S., Signal, B., & Processing, I. (2010). Rheometric Studies on Agarose Gel - A Brain Mimic Material. SASTech Technical Journal, 9(2), 27–30.

Destrade, M., Saccomandi, G., & Sgura, I. (2017). Methodical fitting for mathematical models of rubber-like materials. Proceedings of the Royal Society A: Mathematical, Physical and Engineering Sciences, 473(2198), 20160811. doi:10.1098/rspa.2016.0811.

Dormoy, Y., & Candau, S. (1991). Transient electric birefringence study of highly dilute agarose solutions. *Biopolymers*, 31(1), 109-117. doi:10.1002/bip. 360310110

El-Sherbiny, I. M., & Yacoub, M. H. (2013). Hydrogel scaffolds for tissue engineering: Progress and challenges. Global Cardiology Science and Practice, 2013(3), 316–342. doi:10.5339/gcsp.2013.38.

Faturechi, R., Karimi, A., Hashemi, A., Yousefi, H., & Navidbakhsh, M. (2015). Influence of Poly(acrylic acid) on the mechanical properties of composite hydrogels. *Advances in Polymer Technology*, 34(2), 1–7. doi:10.1002/adv.21487.

Forte, A. E., Galvan, S., Manieri, F., Rodriguez y Baena, F., & Dini, D. (2016). A composite hydrogel for brain tissue phantoms. *Materials & Design*, 112, 227–238. doi:10.1016/j.matdes.2016.09.063.

Fujii, T., Yano, T., Kumagai, H., & Miyawaki, O. (2000). Scaling analysis of the concentration dependence on elasticity of Agarose gel. Bioscience, Biotechnology, and Biochemistry, 64(8), 1618–1622. doi:10.1271/bbb.64.1618.

Gent, A. N. (1996). A new constitutive relation for rubber. Rubber Chemistry and Technology, 69(1), 59-61. doi:10.5254/1.3538357.

Guenet, J.-. M. (2000). Structure versus rheological properties in fibrillar thermoreversible gels from polymers and biopolymers. *Journal of Rheology*, 44(4), 947–960. doi:10.1122/1.551121.

Guenet, J. M., & Rochas, C. (2006). Agarose sols and gels revisited. Macromolecular Symposia, 242, 65-70. doi:10.1002/masy.200651011.

Hinkley, J. A., Morgret, L. D., & Gehrke, S. H. (2004). Tensile properties of two responsive hydrogels. *Polymer*, 45(26), 8837–8843. doi:10.1016/j.polymer.2004. 09.088.

Horgan, C. O., & Saccomandi, G. (2003). Finite thermoelasticity with limiting chain extensibility. *Journal of the Mechanics and Physics of Solids*, 51(6), 1127–1146. doi:10.1016/S0022-5096(02)00144-8.

Hyon, S.-. H., Cha, W.-. I., Ikada, Y., Kita, M., Ogura, Y., & Honda, Y. (1994). Poly(vinyl alcohol) hydrogels as soft contact lens material. *Journal of Biomaterials Science, Polymer Edition*, 5(5), 397–406. doi:10.1163/156856294x00103.

Jones, J. L., & Marques, C. M. (1990). Rigid polymer network models. Journal de Physique, 51(11), 1113-1127. doi:10.1051/jphys:0199000510110111300.

Kim, H., Kim, B. Y., Gunasekaran, S., Park, J. W., & Yoon, W. B. (2013). Comparison of concentration dependence of mechanical modulus in two biopolymer gel systems using scaling analysis. Food Science and Biotechnology, 22(6), 1601–1606. doi:10.1007/s10068-013-0256-9.

Kwon, H. J., Rogalsky, A. D., Kovalchick, C., & Ravichandran, G. (2010). Application of digital image correlation method to biogel. *Polymer Engineering & Science*, 50(8), 1585–1593. doi:10.1002/pen.21636.

Leclerc, G. E., Debernard, L., Foucart, F., Robert, L., Pelletier, K. M., & Charleux, F., Ehman, R., Ho Ba Tho, M. C., & (2012). Characterization of a hyperviscoelastic phantom mimicking biological soft tissue using an abdominal pneumatic driver with magnetic resonance elastography (MRE). *Journal of Biomechanics*, 45(6), 952–957. doi:10.1016/j.jbiomech.2012.01.017.

Liljenhjerte, J., Upadhyaya, P., & Kumar, S. (2016). Hyperelastic strain measurements and constitutive parameters identification of 3D printed soft polymers by image processing. *Additive Manufacturing*, 11, 40–48. doi:10.1016/j.addma.2016.03.005.

Lin, C. C., & Anseth, K. S. (2009). PEG hydrogels for the controlled release of biomolecules in regenerative medicine. *Pharmaceutical Research*, 26(3), 631–643. doi:10.1007/s11095-008-9801-2.

Luo, K., Upadhyay, K., Subhash, G., & Spearot, D. E. (2019). Transient-state rheological behavior of Poly(ethylene glycol) diacrylate hydrogels at high shear strain rates. *Macromolecules*, 52(15), 5860–5871. doi:10.1021/acs.macromol.9b00820.

Ma, P. X. (2004). Scaffolds for tissue fabrication. Materials Today, 7(5), 30-40. doi:10.1016/S1369-7021(04)00233-0.

Marckmann, G., & Verron, E. (2006). Comparison of hyperelastic models for rubber-like materials. Rubber Chemistry and Technology, 79(5), 835–858. doi:10. 5254/1.3547969.

Mathews, D. T., Birney, Y. A., Cahill, P. A., & McGuinness, G. B. (2008). Mechanical and morphological characteristics of poly(vinyl alcohol)/chitosan hydrogels. Journal of Applied Polymer Science, 109(2), 1129–1137. doi:10.1002/app.28104.

Maxwell, A. D., Wang, T. Y., Yuan, L., Duryea, A. P., Xu, Z., & Cain, C. A. (2010). A tissue phantom for visualization and measurement of ultrasound-induced cavitation damage. *Ultrasound in Medicine and Biology*, 36(12), 2132–2143. doi:10.1016/j.ultrasmedbio.2010.08.023.

Moerman, K. M., Holt, C. A., Evans, S. L., & Simms, C. K. (2009). Digital image correlation and finite element modelling as a method to determine mechanical properties of human soft tissue in vivo. *Journal of Biomechanics*, 42(8), 1150–1153. doi:10.1016/j.jbiomech.2009.02.016.

Mooney, M. (1940). A theory of large elastic deformation. Journal of Applied Physics, 11(9), 582-592. doi:10.1063/1.1712836.

Moura, M. J., Figueiredo, M. M., & Gil, M. H. (2007). Rheological study of genipin cross-linked chitosan hydrogels. *Biomacromolecules*, 8(12), 3823–3829. doi:10.1021/bm700762w.

Muliana, A., Rajagopal, K. R., Tscharnuter, D., Schrittesser, B., & Saccomandi, G. (2018). determining material properties of natural rubber using fewer material moduli in virtue of a novel constitutive approach for elastic bodies. *Rubber Chemistry and Technology*, 91(2), 375–389. doi:10.5254/RCT.18.81675.

Naarayan, S. S., & Subhash, G. (2017). Wave propagation in ballistic gelatine. Journal of the Mechanical Behavior of Biomedical Materials, 68(October 2016), 32-41. doi:10.1016/j.jmbbm.2017.01.030.

Normand, V., Lootens, D. L., Amici, E., Plucknett, K. P., & Aymard, P. (2000). New insight into agarose gel mechanical properties. *Biomacromolecules*, 1(4), 730–738. doi:10.1021/bm005583j.

Ogden, R. W., Saccomandi, G., & Sgura, I. (2004). Fitting hyperelastic models to experimental data. Computational Mechanics, 34(6), 484–502. doi:10.1007/s00466-004-0593-v.

Oyen, M. L. (2014). Mechanical characterisation of hydrogel materials. *International Materials Reviews*, 59(1), 44–59. doi:10.1179/1743280413Y.0000000022. Pasumarthy, R. K. A., & Tippur, H. V. (2016). Mechanical and optical characterization of a tissue surrogate polymer gel. *Polymer Testing*, 55, 219–229. doi:10. 1016/i.polymertesting.2016.08.004.

Pavan, T. Z., Madsen, E. L., Frank, G. R., Adilton O Carneiro, A., & Hall, T. J. (2010). Nonlinear elastic behavior of phantom materials for elastography. *Physics in Medicine and Biology*, 55(9), 2679–2692. doi:10.1088/0031-9155/55/9/017.

Peattie, R. A., Nayate, A. P., Firpo, M. A., Shelby, J., Fisher, R. J., & Prestwich, G. D. (2004). Stimulation of in vivo angiogenesis by cytokine-loaded hyaluronic acid hydrogel implants. *Biomaterials*, 25(14), 2789–2798. doi:10.1016/j.biomaterials.2003.09.054.

Pervin, F., & Chen, W. W. (2011). In T. Proulx (Ed.). In Dynamic behavior of materials, volume 1. conference proceedings of the society for experimental mechanics series: 1 (pp. 9–13). Springer. doi:10.1007/978-1-4419-8228-5_3.

Pomfret, R., Miranpuri, G., & Sillay, K. (2013). The substitute brain and the potential of the gel model. Annals of Neurosciences, 20(3), 118-122. doi:10.5214/ans.0972.7531.200309.

Pucci, E., & Saccomandi, G. (2002). A Note on the gent model for rubber-like materials. Rubber Chemistry and Technology, 75(5), 839-852. doi:10.5254/1. 3547687.

Puglisi, G., & Saccomandi, G. (2016). Multi-scale modelling of rubber-like materials and soft tissues: An appraisal. Proceedings of the Royal Society A: Mathematical, Physical and Engineering Sciences, 472(2187), 20160060. doi:10.1098/rspa.2016.0060.

Rajagopal, K. R. (2003). On implicit constitutive theories. Applications of Mathematics, 48(4), 279-319. doi:10.1023/A:1026062615145.

Rajagopal, K. R. (2007). The elasticity of elasticity. Zeitschrift Für Angewandte Mathematik Und Physik, 58(2), 309-317. doi:10.1007/s00033-006-6084-5.

Ramzi, M., Rochas, C., & Guenet, J. M. (1998). Structure-properties relation for agarose thermoreversible gels in binary solvents. *Macromolecules*, 31(18), 6106–6111. doi:10.1021/ma9801220.

Ratajska-Gadomska, B., & Gadomski, W. (2004). Water structure in nanopores of agarose gel by Raman spectroscopy. *The Journal of Chemical Physics*, 121(24), 12583. doi:10.1063/1.1826051.

Righetti, P. G., Brost, B. C. W., & Snyder, R. S. (1981). On the limiting pore size of hydrophilic gels for electrophoresis and isoelectric focussing. *Journal of Biochemical and Biophysical Methods*, 4, 347–363. doi:10.1016/0165-022X(81)90075-0.

Rinaudo, M. (1993). Gelation of Polysaccharides. Journal of Intelligent Material Systems and Structures, 4(2), 210-215. doi:10.1177/1045389x9300400210.

Rivlin, R. S. (1948). Large elastic deformations of isotropic materials. IV. Further developments of the general theory. *Philosophical Transactions of the Royal Society A: Mathematical, Physical and Engineering Sciences*, 241(835), 379–397. doi:10.1098/rsta.1948.0024.

Rochas, C., Brûlet, A., & Guenet, J. M. (1994). Thermoreversible gelation of Agarose in water/dimethyl sulfoxide mixtures. *Macromolecules*, 27(14), 3830–3835. doi:10.1021/ma00092a023.

Sasson, A., Patchornik, S., Eliasy, R., Robinson, D., & Haj-Ali, R. (2012). Hyperelastic mechanical behavior of chitosan hydrogels for nucleus pulposus replacement-Experimental testing and constitutive modeling. *Journal of the Mechanical Behavior of Biomedical Materials*, 8, 143–153. doi:10.1016/j.jmbbm. 2011.12.008.

Stauffer, D., Coniglio, A., & Adam, M. (1982). Gelation and Critical Phenomena. In in Polymer Networks: 44 (pp. 103–158). BerlinHeidelberg: Springer. doi:10.1007/3-540-11471-8_4.

Subhash, G., Kwon, J., Mei, R., & Moore, D. F. (2012). Non-newtonian behavior of ballistic gelatin at high shear rates. Experimental Mechanics, 52(6), 551–560. doi:10.1007/s11340-011-9513-0.

Subhash, G., Liu, Q., Moore, D. F., Ifju, P. G., & Haile, M. A. (2011). Concentration dependence of tensile behavior in Agarose gel using digital image correlation. Experimental Mechanics, 51(2), 255–262. doi:10.1007/s11340-010-9354-2.

Tang, J., Tung, M. A., Lelievre, J., & Zeng, Y. (1997). Stress-strain relationships for gellan gels in tension, compression and torsion. *Journal of Food Engineering*, 31(4), 511–529. doi:10.1016/S0260-8774(96)00087-8.

Tobajas, R., Ibartz, E., & Gracia, L. (2016). A comparative study of hyperelastic constitutive models to characterize the behavior of a polymer used in automotive engines. *Proceedings of 2nd International Electronic Conference on Materials*, A002. doi:10.3390/ecm-2-A002.

Tokita, M., & Hikichi, K. (1987). Mechanical studies of sol-gel transition: Universal behavior of elastic modulus. *Physical Review A*, 35(10), 4329–4333. doi:10.1103/PhysRevA.35.4329.

Trinh, T. Q., Sorber, J., & Gerlach, G. (2009). Design, simulation and experimental characteristics of hydrogel-based piezoresistive pH sensors. In Springer proceedings in physics: 127 (pp. 287–294). BerlinHeidelberg: Springer. doi:10.1007/978-3-540-88201-5_33.

Upadhyay, K., Bhattacharyya, A., Subhash, G., & Spearot, D. E. (2019a). Quasi-static and high strain rate simple shear characterization of soft polymers. Experimental Mechanics, 59(5), 733–747. doi:10.1007/s11340-019-00507-1.

Upadhyay, K., Subhash, G., & Spearot, D. (2019b). Thermodynamics-based stability criteria for constitutive equations of isotropic hyperelastic solids. *Journal of the Mechanics and Physics of Solids*, 124, 115–142. doi:10.1016/j.jmps.2018.09.038.

Upadhyay, K., Subhash, G., & Spearot, D. (2020). Visco-hyperelastic constitutive modeling of strain rate sensitive soft materials. *Journal of the Mechanics and Physics of Solids*, 135, 103777. doi:10.1016/j.jmps.2019.103777.

Veronda, D. R., & Westmann, R. A. (1970). Mechanical characterization of skin-Finite deformations. Journal of Biomechanics, 3(1), 111-124. doi:10.1016/0021-9290(70)90055-2.

Wang, M., & Kornfield, J. A. (2012). Measuring shear strength of soft-tissue adhesives. Journal of Biomedical Materials Research Part B: Applied Biomaterials, 100B(3), 618-623. doi:10.1002/jbm.b.31981.

Watase, M., & Nishinari, K. (1983). Rheological properties of agarose gels with different molecular weights. Rheologica Acta, 22(6), 580-587. doi:10.1007/BF01351404.

Wex, C., Arndt, S., Stoll, A., Bruns, C., & Kupriyanova, Y. (2015). Isotropic incompressible hyperelastic models for modelling the mechanical behaviour of biological tissues: A review. Biomedical Engineering / Biomedizinische Technik, 60(6), 577–592. doi:10.1515/bmt-2014-0146.

Zhang, J., & Rochas, C. (1990). Interactions between agarose and κ -carrageenans in aqueous solutions. *Carbohydrate Polymers*, 13(3), 257–271. doi:10.1016/0144-8617(90)90058-Z.